Interfacial Chemical Bond and Internal Electric Field Modulated Z-Scheme Vs-ZnIn$_2$S$_4$/MoSe$_2$ Photocatalyst for Efficient Hydrogen Evolution

Xuehua Wang
  Qingdao University of Science and Technology

Xianghu Wang
  Qingdao University of Science and Technology

Jianfeng Huang
  Shaanxi University of Science and Technology

Shaoxiang Li
  Qingdao University of Science and Technology

Alan meng
  Qingdao University of Science and Technology

Zhenjiang Li (✉ zhenjiangli@qust.edu.cn)
  Qingdao University of Science and Technology   https://orcid.org/0000-0001-7636-2962

Article

Abstract

Construction of Z-scheme heterostructure is of momentous significance for realizing efficient photocatalytic water splitting. However, the consciously modulate of Z-scheme charge transfer is still a great challenge. Herein, interfacial Mo-S bond and internal electric field modulated Z-Scheme heterostructure composed by sulfur vacancies-rich ZnIn2S4 (Vs-ZIS) and MoSe2 was rationally fabricated for efficient photocatalytic hydrogen evolution. Systematic investigations reveal that Mo-S bond and internal electric field induce the Z-scheme charge transfer mechanism as confirmed by the SPS and DMPO spin-trapping EPR spectra. Under the intense synergy among the Mo-S bond, internal electric field and S-vacancies, the optimized photocatalyst exhibits ultrahigh hydrogen evolution rate of 63.21 mmol•g-1·h-1 with an apparent quantum yield of 76.48% at 420 nm monochromatic light, which is about 18.8-fold of the pristine ZIS. This work affords a new inspiration on consciously modulating Z-scheme charge transfer by atomic-level interface control and internal electric field to signally promote the photocatalytic performance.

Introduction

With the rapid development of the industrial society, the energy crisis and environmental pollution issues are becoming increasing. Therefore, finding an alternative energy source is of great significance for the long-term development of human society. Hydrogen (H_2) has long been considered as an excellent candidate to substitute the fossil fuel, due to its advantages of clean, renewable, high energy density and transportability[1-3]. However, at present, the low efficiency, high energy consumption and environmentally hazardous H_2 production technology seriously restrict the commercial application of hydrogen energy. By comparison, photocatalytic water splitting can tactfully convert the sustainable solar energy to H_2 energy without discharging any pollutant during the whole process, thus has been considered as a sustainable and promising technique[4-6].

According to the photocatalytic reaction principle, the efficient photocatalyst should possess the sufficient light absorption, the effective photocarriers separation and transfer, and the accelerated surface redox reaction. However, for mono-component semiconductor, it is impossible to satisfy all of these demands at the same time. Over the past decades, researchers have developed various strategies to improve photocatalytic property, including phase and morphology regulating, elements doping, cocatalyst-loading, defect engineering and heterojunction constructing[7-11]. Among these strategies, defect engineering and heterojunction constructing are the two-effective means. In photocatalytic field, introducing appropriate concentration of anion vacancies in semiconductor can not only enhance the light absorption ability of the pristine semiconductor, but also introduce mid gap states in the band gap, which can serve as effective electron "traps" accelerating the separation efficiency of photocarriers[12]. For example, Dai et al. synthesized a N-deficient g-C_3N_4, which exhibits about 3-fold photocatalytic H_2 evolution (728 µmol•g^{-1}•h^{-1}) of the pristine g-C_3N_4[13]. Chen et al. prepared a hydrogenated $ZnIn_2S_4$ (H-ZIS) microspheres with sulfur vacancies for photocatalytic H_2 evolution. The results demonstrates that the

hydrogen evolution rate of H-ZIS is as high as 1.9 mmol•g^{-1}•h^{-1} (nearly 8.6 times that of the pristine ZIS sample)[14]. However, as known from the reported literatures, the only defects introduction is not enough for realizing efficient photocatalytic property.

Heterojunction constructed by coupling different materials with diverse energy level structure is another effective means to improve photocatalytic performance[15-17]. In recent years, Z-scheme heterostructure, especially the direct Z-scheme heterostructure, has become one of the most effective strategy for obtaining high-efficient photocatalyst [18,19]. To fabricate the Z-scheme heterostructure, the primary premise is the matching band structure, in which the conduction band of one semiconductor should locate as close to the valence band of another semiconductor as possible. Nevertheless, the suitable band structure is insufficient for Z-scheme charge transfer. For example, it is reported that the conduction band potential of MoSe$_2$ (about -0.45 eV[20]) is lower than the conduction band of ZnIn$_2$S$_4$, but very close to its valence band (0.99 eV[21]), which suggests that the photogenerated electrons on the conduction band of MoSe$_2$ are likely to recombine with the photogenerated holes on the valence band of ZnIn$_2$S$_4$ following Z-scheme pathway. However, as known from the current literatures, MoSe$_2$ can only play the role of cocatalyst in ZnIn$_2$S$_4$/MoSe$_2$ instead of realizing Z-scheme charge transfer[22,23]. The question is that there is no direct and intimate interfacial connection between MoSe$_2$ and ZnIn$_2$S$_4$. The poor interfacial contact is like erecting a "wall" between the two semiconductors, seriously preventing the trajection of charge flow. Therefore, the formation of intimate interface contact became the hinge to Z-scheme photocatalyst fabrication.

Recently, defect-induced heterostructure construction have opened a new thought for assembling the heterostructure with specific atomic-level interfacial contact[18]. Its basic principle lies on that the defective sites with abundant coordinative unsaturation atoms and delocalize local electrons can act as the anchoring sites for other semiconductors to form a unique heterostructure contact interface with chemical bond connection[24]. The interfacial chemical bond can act as specific "bridge" accelerating charge transfer between semiconductors. In addition to the intimate interface combination, internal electric field also emerging as a viable strategy to promote Z-scheme charge transfer[25]. Under the effect of internal electric field, the photogenerated electrons in the conduction band of one semiconductor with lower Fermi level could directionally transfer to the valence band of another semiconductor with higher Fermi level, thus realizing the Z-scheme charge transfer[26]. Inspired by the above considerations, an efficient Z-scheme photocatalyst can be obtained through establishing intimate interfacial chemical bond connection between two semiconductors with specific band structure and Fermi level. Up to now, however, the interfacial bonding and internal electric field are always considered separately, the jointly modulation and their synergy effect on photocatalytic performance still remains a challenging task.

Herein, taking S vacancies-rich ZnIn$_2$S$_4$ and MoSe$_2$ as model material, through a defect-induced heterostructure constructing strategy, an interfacial Mo-S bond and internal electric field modulated Z-scheme Vs-ZnIn$_2$S$_4$/MoSe$_2$ photocatalyst was fabricated for the first time. The addition of hydrazine

monohydrate ($N_2H_4 \cdot H_2O$) provides pivotal prerequisite for the formation of S vacancies (Vs) and coordinative unsaturation S atoms, where the S vacancies can enhance light absorption and facilitate photocarriers separation, while the abundant coordinative unsaturation S atoms can serve as anchoring sites for Mo atoms, thus contributing the formation of Mo-S bond and the in-situ growth of $MoSe_2$ on the surface of Vs-$ZnIn_2S_4$ (as showing in Fig.1). During photocatalytic reaction, the internal electric field induced by the different work function between Vs-$ZnIn_2S_4$ and $MoSe_2$ provide intense driving force steering the photogenerated electrons on the conduction band of $MoSe_2$ transfer to the valence band of Vs-$ZnIn_2S_4$, that's the Z-scheme mechanism. Meanwhile, the interfacial Mo-S bond afford the fast pathways for charge transfer from $MoSe_2$ to Vs-$ZnIn_2S_4$, thus accelerating the Z-scheme charge transfer process. This work provides a constructive reference for atomic-level interfacial and internal electric field regulating Z-scheme heterostructure for efficient photocatalytic reaction.

Results And Discussion

Characterization of as of as-prepared photocatalysts. The morphology and microstructure of the as-synthesized ZIS, $MoSe_2$ and Vs-ZIS/$MoSe_2$ (the optimized sample) were analyzed by the SEM, TEM and HRTEM characterizations. As observed in Fig. 2a, the basic morphology of ZIS is flower-like hierarchical microsphere composed by plenty of intersecting nanoflakes, which benefits to the exposure of active surface. The TEM image in Fig. 2b further reveals the hierarchical microsphere of ZIS assembled by nanoflakes. Furtherly, as shown in the HRTEM image in Fig. 2c, the clear lattice stripes with interplanar spacing (d) of 0.32 nm can be well indexed to the (102) lattice plane of hexagonal $ZnIn_2S_4$ (JCPDS:65-2023)[14]. Fig. S1-S2 are the elements mapping and EDS spectrum of ZIS, it can be clearly seen the evenly distributed Zn, In and S elements, and the atomic ratio of Zn/In/S can be calculated to be about 1.00/1.85/4.13 (as listed in Table S1), very close to the stoichiometric ratio of $ZnIn_2S_4$. Fig. S3 presents the SEM, TEM and element mapping images of the S vacancies-rich ZIS (Vs-ZIS). It is found that the Vs-ZIS appears the identical morphology and structure with ZIS, suggesting that the $N_2H_4 \cdot H_2O$-assisted hydrothermal treatment cannot destroy the flower-like microsphere structure of ZIS. The atomic ratio of Zn/In/S in Vs-ZIS sample is approximately 1.00/1.92/3.35 (as displayed in Table S2), the distinctly deficient of S atom compared to that in ZIS confirms the existence of abundant S vacancies in ZIS. Fig. 2d is the TEM picture of $MoSe_2$, which manifests the nanosheet feature. The HRTEM image (Fig. 2e and f) present the d-spacing of 0.65 and 0.24 nm, assigning to the (002) and (103) lattice planes of 2H-$MoSe_2$ (JCPDS: 29-0914), respectively[27]. Fig. 2g is the SEM image of Vs-ZIS/$MoSe_2$, which exhibits almost the same morphology with ZIS, moreover, the ZIS and $MoSe_2$ in the Vs-ZIS/$MoSe_2$ structure are undistinguishable, indicating that the $MoSe_2$ was grown on the surface of ZIS intimately to form a 2D/2D contact, and the introduction of $MoSe_2$ can hardly affect the hierarchical microsphere morphology of ZIS. The TEM image displaying in Fig. 2h and i further reveal the hierarchical flower-like microsphere structure of Vs-ZIS/$MoSe_2$, which could lead to the enhanced light absorption by the multilevel reflection and scattering of the incident light[28]. Furthermore, the HRTEM picture displaying in Fig. 2j shows the different lattice stripes with d value of 0.32 and 0.24 nm, respectively, which can be indexed to the (102) crystal

face of hexagonal $ZnIn_2S_4$ (JCPDS:65-2023) and the (103) lattice planes of 2H-$MoSe_2$ (JCPDS: 29-0914), respectively. The HRTEM results indicate that $MoSe_2$ are directly grown and attach on the ZIS nanosheets substrate. Fig. 2k-p are the EDS spectra and element mapping of Vs-ZIS/$MoSe_2$, as displayed, the distribution of Zn, In, S elements are dense and uniform, meanwhile, the Mo and Se elements are relatively sparse but still evenly distributed. From the EDS spectrum, the mass ratio of $MoSe_2$ to ZIS can be calculated to be about 4.8% (as presented in Table S4), which is very close to the ratio of the added raw materials. What's more, the atomic ratio of Zn/In/S in Vs-ZIS/$MoSe_2$ was determined to be 1.00/1.83/3.25, indicating that there is still a mass of S vacancies inside Vs-ZIS/$MoSe_2$.

The ZIS, Vs-ZIS, $MoSe_2$ and Vs-ZIS/$MoSe_2$ were further characterized by X-ray diffraction (XRD) to determine the phase composition. As displayed in Fig. 2q, the XRD pattern of $MoSe_2$ matches well with 2H-$MoSe_2$ (JCPDS:29-0914)[23]. Meanwhile, ZIS displays the distinct peaks at 21.6°, 27.7°, 30.4°, 39.8°, 47.2°, 52.4°, 55.6° and 76.4°, which can be severally indexed to the (006), (102), (104), (108), (110), (116), (022) and (213) crystal planes of hexagonal $ZnIn_2S_4$ (JCPDS:65-2023)[28]. It is worth noting that the Vs-ZIS sample shows almost the same XRD pattern with ZIS, indicating that the introduction of S vacancies can hardly affect the size and crystal structure of ZIS. Moreover, in the XRD patterns of Vs-ZIS/$MoSe_2$, in addition to the peaks of hexagonal ZIS, a new peak at about 13.7° can be well assigned to the (002) crystal face of $MoSe_2$, reconfirming the successful synthesis of Vs-ZIS/$MoSe_2$ composite.

To further characterize the chemical structures of the as-synthesized photocatalyst, the Raman spectra were carried out (shown in Fig. 2r). As observed in the Raman spectra of $MoSe_2$, the peaks located at 235.4, 277.4 and 330.8 cm^{-1} stem from the A_{1g}, E_{2g} and B_{2g} modes of 2H-$MoSe_2$, respectively, while the peak at 142.1 cm^{-1} is associated to the E_{1g} mode of the in-plane bending of Se atoms in 2H-$MoSe_2$[29]. For the Raman spectra of Vs-ZIS, the peaks located at 244.8 and 348.9 cm^{-1} can be severally assigned to the F_{2g} and A_{1g} modes of $ZnIn_2S_4$. Furtherly, as for the Vs-ZIS/$MoSe_2$ (the red line), in addition to the E_{1g} mode of 2H-$MoSe_2$, and the F_{2g} and A_{1g} modes of $ZnIn_2S_4$, a new emerging peak situated at about 404.9 cm^{-1} can be indexed to the Mo-S bonding state[30], suggesting that the Vs-ZIS and $MoSe_2$ were combined intimately by Mo-S bond. Additionally, it can be observed that all the peaks in Vs-ZIS/$MoSe_2$ exhibited evidently blue-shift compared to that in Vs-ZIS, further revealing the intense chemical coupling effect between the Vs-ZIS and $MoSe_2$[31].

To further testify the existence of S vacancies, the electron paramagnetic resonance (EPR) was carried out (Fig. 2s). For the original ZIS sample, the EPR intensity can hardly be observed, in comparison, the Vs-ZIS sample shows the sharply increased EPR signal at a g-factor of 2.009, confirming the abundant S-vacancies in Vs-ZIS[32,33]. In addition, it is interesting to observe that the EPR intensity of Vs-ZIS/$MoSe_2$ exhibits slightly decreased compared to that of Vs-ZIS, which should be contributed to the bonding effect among Mo and unsaturated S in Vs-ZIS, decreasing the number of unpaired electrons, but the S vacancies in ZIS haven't been sewed up by compositing $MoSe_2$[34].

The X-ray photoelectron spectroscopy (XPS) was applied to investigate the surface composition and chemical states of ZIS, Vs-ZIS and Vs-ZIS/MoSe$_2$, and the results are showing in Fig. 3. As can be found from the survey spectrum (Fig. 3a), the Zn, In and S peaks are coexisting in ZIS and Vs-ZIS, in comparison, Mo and Se peaks can also be observed in the Vs-ZIS/MoSe$_2$, which is agree with the EDS test results. As observed in Fig. 3b, the S 2p$_{3/2}$ and 2p$_{1/2}$ of the original ZIS located at 161.72 and 162.97 eV, respectively, in accordance with the reported literature[33]. In comparison, the S 2p$_{3/2}$ and 2p$_{1/2}$ of Vs-ZIS presented evident negative-shift of about 0.14 eV and 0.19 eV, respectively, verifying the generation of S vacancies in ZIS. The S-vacancies can serve as strong electron-withdrawing group for facilitating the ZIS electrons transfer to S-vacancies, thus decreasing the equilibrium electron cloud density of S atoms inside ZIS, and further leading to the decreased binding energy[35,36]. Furtherly, it can be noted that the S 2p$_{3/2}$ and 2p$_{1/2}$ of Vs-ZIS/MoSe$_2$ exhibited a positive-shift of about 0.13 and 0.17 eV compared to that of Vs-ZIS, which should be caused by the strong interfacial interaction between MoSe$_2$ and Vs-ZIS[31]. Besides, as shown in Fig. 3c and d, the Zn 2p and In 3d in Vs-ZIS also exhibited a slightly negative-shift compared to that in ZIS, which could be explained that the generation of S vacancies leading to the decreased coordination number of Zn and In[28].After combining with MoSe$_2$, the Zn 2p and In 3d peaks re-shift to the high binding energy region, revealing that the bonding effect between Mo atoms in MoSe$_2$ and unsaturated coordination S in Vs-ZIS contributing to the slightly increased electron cloud density around Zn and In. Interestingly, it can also be observed that the binding energy variation of Zn 2p in ZIS, Vs-ZIS and Vs-ZIS/MoSe$_2$ are more notable than that of In 3d, revealing that the Mo were mainly bonded with the S around Zn sites[34]. What's more, according to the XPS peak area, the actual atomic ratio of Zn/In/S in ZIS, Vs-ZIS and Vs-ZIS/MoSe$_2$ are 1.00/2.15/3.87, 1.00/2.20/3.29 and 1.00/2.14/3.36, respectively. The lower S atom ratio in Vs-ZIS and Vs-ZIS/MoSe$_2$ further confirm the presence of abundant S vacancies. As shown in Fig. 3e, the peaks at 228.05 and 230.5 eV can be attributed to Mo 3d$_{5/2}$ and 3d$_{3/2}$ of Mo^{4+} in MoSe$_2$, meanwhile, the peak at 227.1 eV verified the formation of Mo-S bond[38]. Fig. 3f is the Mo 3p spectrum, as observed, four distinct XPS peaks can be distinguished, where the peaks at 400.55 and 390.3 eV can be corresponded to the Se Auger peaks, and the peaks at 395 and 416 eV can be assigned to the Mo 3p$_{3/2}$ and 3p$_{1/2}$ of Mo^{4+}. The Se 3d spectrum presented in Fig. 3g shows two peaks at 54.4 and 55.35 eV, which can be indexed to Se 3d$_{5/2}$ and 3d$_{3/2}$ of Se^{2-} in MoSe$_2$, respectively[39]. The XPS results further confirm the successful synthesis of Vs-ZIS and Vs-ZIS/MoSe$_2$ with abundant S-vacancies, and the MoSe$_2$ is attached on the surface of Vs-ZIS through Mo-S bond.

Photocatalytic H$_2$ evolution activity measurements. The photocatalytic H$_2$ evolution were evaluated under the visible light (λ>420 nm) irradiation, the corresponding test results are showing in Fig. 4. As shown in Fig. 4a and b, all the tested samples exhibit H$_2$ production activity except for MoSe$_2$. The pristine ZIS exhibits the poor H$_2$ production activity of about only 3.36 mmol•g^{-1}·h^{-1}, in comparison, the Vs-ZIS presents a slightly improved H$_2$ evolution rate of 4.77 mmol•g^{-1}·h^{-1}. The improved photocatalytic performance of Vs-ZIS should be ascribed to the accelerated photocarriers separation induced by S vacancies as the electrons trap. Furtherly, the introduction of MoSe$_2$ gave rise to the distinctly improved

H_2 evolution activity, and the H_2 evolution rate of Vs-ZIS/MoSe$_2$ increased with the mass ratio of MoSe$_2$ to ZIS increasing. Until the mass ratio of MoSe$_2$ to ZIS reaches to 5.0%, the H_2 evolution rate reaches to the highest of 63.21 mmol•g^{-1}·h^{-1}, which is about 18.8 and 13.3 times higher than that of pristine ZIS and Vs-ZIS, respectively, and superior to the recently reported ZnIn$_2$S$_4$-based photocatalytic system (as listed in Table S6). It can also be observed that the Vs-ZIS-5.0MoSe$_2$ (synthesized by mixing Vs-ZIS and MoSe$_2$ by ultrasound) performs obvious inferior H_2 evolution property compared to that of Vs-ZIS/5.0MoSe$_2$, indicating that the in-situ growth of MoSe$_2$ on Vs-ZIS connecting by Mo-S bond plays critical influence on the photocatalytic performance of the ZIS-MoSe$_2$ composite, which should be attributed to that the Mo-S bond could facilitate the charge transfer between Vs-ZIS and MoSe$_2$. Fig. S6 shows the wavelength dependent hydrogen evolution efficiency of Vs-ZIS/MoSe$_2$, and the corresponding test results and the light power of different monochromatic light are displaying in Table S5. The apparent quantum yield (AQY) of photocatalytic H_2 evolution can be calculated (the detailed calculation process is shown in the Supporting Information) and displayed in Fig. 4c. As observed, the AQY values are about 93.08% (380 nm), 76.48% (420 nm), 29.7% (500 nm) and 0.15% (600 nm), match well with the UV-vis absorption spectra, indicating the outstanding optical absorption and utilization capacity of Vs-ZIS/MoSe$_2$ photocatalyst. In addition to the excellent photocatalytic H_2 evolution efficiency, the recycling stability is also a pivotal factor for the practical application of photocatalyst. As discerned in Fig. 4d, the H_2 evolution amount of the optimized Vs-ZIS/MoSe$_2$ photocatalyst remains about 90.5% after 20 hours of 5 cycles of photocatalytic tests, signifying the excellent photocatalytic stability of Vs-ZIS/MoSe$_2$ photocatalyst, which maybe contributed to the favorable anti-photocorrosion ability of Vs-ZIS/MoSe$_2$, and the strong combination between ZIS and MoSe$_2$.

Photophysical and Electrochemical Properties. Fig. 5a is the UV-vis absorption spectra of ZIS, Vs-ZIS, MoSe$_2$ and Vs-ZIS/MoSe$_2$. It is apparent that the MoSe$_2$ shows the intense light absorption in the whole UV-vis light range, which should be caused by its dark black color. Meanwhile, it can be observed that light absorption intensity of Vs-ZIS is higher than that of ZIS, indicating that the introduction of S vacancies can influence the band structure of ZIS. Furtherly, after combining with MoSe$_2$, the light absorption of Vs-ZIS/MoSe$_2$ increased again compared to Vs-ZIS. The improved light absorption is in favor of the generation of photocarriers, and beneficial for the enhancement of photocatalytic performance[21]. Fig. 5b is the PL spectroscopy. As displayed, under the 375 nm excitation wavelength, the pristine ZIS displays a prominent emission peak, indicating the intense recombination of photogenerated carriers inside ZIS. In comparison to ZIS, the emission peak intensity of Vs-ZIS decreases lightly, which should be contributed to that S vacancies can act as electrons trap for facilitating the photocarriers separation. It is worth noting that the PL signal of Vs-ZIS/MoSe$_2$ sample is further quenched compared to that of Vs-ZIS, revealing the positive effect of MoSe$_2$ for suppressing the recombination of photocarriers. Fig. 5c is the photocurrent response. As observed, all the tested samples exhibit the light-response characteristic under the FX-300 Xe lamp. Obviously, the photocurrent density is in the order of Vs-ZIS/MoSe$_2$>Vs-ZIS>ZIS. The highest photocurrent density of Vs-ZIS/MoSe$_2$ reveals the most accelerated

photocarriers separation and migration efficiency. Fig. 5d is the electrochemical impedance spectroscopy (EIS). As compared, $MoSe_2$ express the smallest semicircle, meanwhile, the semicircle of ZIS is the largest. Obviously, the semicircle of Vs-ZIS is slightly lower than that of ZIS, and the semicircle of Vs-ZIS/$MoSe_2$ is significantly decreased than that of pristine ZIS and Vs-ZIS, manifesting that the introduction of S vacancies and the combination with $MoSe_2$ can decrease the interfacial charge transfer resistance, which is in favor of photogenerated carriers transfer and separation, and finally facilitate the photocatalytic property.

In order to investigate the effects of the $MoSe_2$ to ZIS mass ratio on the photocatalytic performance of Vs-ZIS/$MoSe_2$ composites. The light absorption, photocarriers separation and photocurrent density of Vs-ZIS/$MoSe_2$ photocatalysts with different mass ratio of $MoSe_2$ to ZIS were also characterized by UV-vis absorption, steady-state PL spectroscopy and photocurrent response. As observed in Fig. S6, with increasing the mass ratio of $MoSe_2$ to ZIS, the light absorption intensity enhance gradually. It is worth mentioning that the Vs-ZIS/7.0$MoSe_2$ sample displays the strongest light absorption ability, but its photocatalytic H_2 production performance is not the best (as known from Fig. 4a), suggesting that the light absorption is not the only decisive factor for the photocatalytic activity. Fig. S7 is the PL spectra, it can be observed that the PL peak of Vs-ZIS/5.0$MoSe_2$ is the lowermost, revealing the most effective photocarriers separation when the mass ratio of $MoSe_2$ to ZIS is 5%, which directly explains why the Vs-ZIS/5.0$MoSe_2$ sample has the best photocatalytic performance. Fig. S8 shows the photocurrent response. As displayed, the Vs-ZIS/5.0$MoSe_2$ shows the highest photocurrent density, which is the result of high-efficiency separation and transfer of photogenerated electron and hole, further revealing the optimum photocatalytic performance of Vs-ZIS/5.0$MoSe_2$. As known from the above results, the prominent photocatalytic performance requires the coordination among the efficient light absorption, photocarrier separation and transfer ability.

Mechanism analysis. Furthermly, the bandgap value (E_g) of the tested sample can be obtained from the Kubelka-Munk function vs. the energy of incident light plots[40]. As displayed in Fig. 6a, the E_g of ZIS, Vs-ZIS and Vs-ZIS/$MoSe_2$ can be estimated to be 2.35, 2.28 and 2.19 eV, respectively. The narrower E_g is beneficial for the incident light absorption and photocarriers generation, thereby contributing to the photocatalytic property[41]. The Mott-Schottky (M-S) plot can be obtained by the following formula of

$$C_{sc}^{-2} = \frac{2}{\varepsilon \varepsilon_0 e N_D} \left(E - E_{fb} - \frac{k_B T}{e} \right),$$

in which C_{SC} represents space charge capacitance, ε represents the dielectric constant, ε_0 represents the permittivity of vacuum, e represents the single electron charge, N_D represents the charge carrier density, E_{fb} represents the flat band potential, k_B represents the Boltzmann constant, and T represents the temperature, E represents the electrode potential[21]. As displayed in Fig. 6b-d, the E_{fb} of ZIS, Vs-ZIS and

MoSe$_2$ can be determined to be -0.96, -0.9 and -0.1 V (vs. NHE), respectively, by extending the linear part of M-S plots. Besides, all the tested samples exhibit the positive slope of M-S plots, indicating the n-type semiconductor traits. As known, the conduction band potential (E$_{CB}$) of n-type semiconductor is approximately 0.2 eV negative than the E$_{fb}$[37], thus the E$_{CB}$ of ZIS, Vs-ZIS and MoSe$_2$ can be discerned to -1.16, -1.1 and -0.3 V (vs. NHE), respectively. According to the equation of E$_{VB}$ = E$_{CB}$ + E$_g$ (E$_{VB}$ is the potential of valence band (VB)), the E$_{VB}$ of the ZIS and Vs-ZIS can be estimated to 1.19 and 1.18 V vs. NHE, respectively. According to the reported literature, the E$_g$ of MoSe$_2$ is about 1.89 eV, therefore, the E$_{VB}$ of MoSe$_2$ can be determined to be 1.59 eV[42].

The work function (Φ) is an important nature for reflecting the escaping ability of free electron from fermi level (E$_f$) to vacuum level[43]. To investigate the mechanism for the excellent photocatalytic performance of Vs-ZIS/MoSe$_2$, the ultraviolet photoelectron spectroscopy (UPS) with He Ⅰ as the excitation source was conducted. As displayed in Fig. 6e, the secondary cutoff binding energy (E$_{cutoff}$) of Vs-ZIS and MoSe$_2$ can be respectively determined as 17.65 and 16.87 eV, by extrapolating the linear part to the base line of the UPS spectra. Based on the formula of Φ=hv-E$_{cutoff}$, the Φ of Vs-ZIS and MoSe$_2$ can be calculated as 3.57 and 4.35 eV, respectively. Hence, the E$_f$ of Vs-ZIS and MoSe$_2$ can be determined as -0.93 and -0.15 V (vs. NHE), respectively. Based on the above calculation and analysis results, the detailed band structure of Vs-ZIS, MoSe$_2$ and Vs-ZIS/MoSe$_2$ were depicted in Fig. 6f. As observed, the E$_f$ of MoSe$_2$ is below that of Vs-ZIS, hence, when Vs-ZIS and MoSe$_2$ contact and form an intimate interface, the free electrons in Vs-ZIS with high E$_f$ would spontaneously diffuse to MoSe$_2$ with low E$_f$, until a new equilibrium state E$_f$ fabricated. The electron drifting from Vs-ZIS to MoSe$_2$ result in the charge redistribution on the interface between Vs-ZIS and MoSe$_2$, in which the interface near Vs-ZIS side is positively charged, while negatively charged near the MoSe$_2$ side, as result, an internal electric field from Vs-ZIS to MoSe$_2$ was built[44].

Accordingly, the photocatalytic reaction mechanism of Vs-ZIS/MoSe$_2$ can be elaborated in Fig. 7a. Under the irradiation of visible light, a mass of photoinduced electrons (e$^-$) with enough energy would transfer from the VB of Vs-ZIS and MoSe$_2$ to the CB of Vs-ZIS and MoSe$_2$, respectively, while the holes (h$^+$) be left on the VB of Vs-ZIS and MoSe$_2$, respectively. It should be mentioned that the abundant S vacancies inside ZIS could introduce new donor level in the band gap of ZIS, which can act as efficient electrons trap to suppress the photogenerated electron-hole pairs recombination[45]. Furtherly, under the driving effect of the internal electric field, the electrons on the CB of MoSe$_2$ would migrate to the VB of Vs-ZIS to recombine with the holes. The Mo-S bond acting as atomic-level interfacial "bridge" can promote the photoexcited carriers migration between Vs-ZIS and MoSe$_2$, thus significantly accelerating the Z-scheme charge transfer. To validate the Z-scheme charge transfer mechanism, the SPV and EPR measurements were carried out. Fig. 7b is the SPV spectra of Vs-ZIS, MoSe$_2$ and Vs-ZIS/MoSe$_2$ samples. It is noted that the pristine MoSe$_2$ presents no SPV signals in the whole wavelength, suggesting the poor photocarriers separation efficiency inside the MoSe$_2$, that's why MoSe$_2$ performed very poor hydrogen evolution. In

comparison, a significant positive photovoltage response can be observed in the SPV spectra of Vs-ZIS, suggesting that the holes migrate to the surface of Vs-ZIS, which is the typical trait of n-type semiconductor[46]. Meanwhile, the SPV response of Vs-ZIS/MoSe$_2$ is significantly lower than that of Vs-ZIS, which means that fewer photogenerated holes migrate to the surface of Vs-ZIS/MoSe$_2$. This phenomenon should be contributed to that the photogenerated electrons on the CB of MoSe$_2$ transfer to the VB of Vs-ZIS and recombine with the photogenerated holes, that's the Z-scheme mechanism[47]. EPR spin-trapping experiment with DMPO as spin-trapping reagent was further proceeded to support the Z-scheme charge transfer mechanism in Vs-ZIS/MoSe$_2$. As displayed in Fig. 7c, almost no DMPO-•O$_2^-$ signals can be observed under dark conditions. However, under visible light irradiation, the characteristic peaks of DMPO-•O$_2^-$ (1:1:1:1) can be monitored for the Vs-ZIS/MoSe$_2$ methanol dispersion liquid, and the peak intensity increase with the time extending, suggesting that the •O$_2^-$ was generated in the reaction system[48]. In theory, the electrons on MoSe$_2$ cannot reduce O$_2$ to product •O$_2^-$ due to the lower CB potential of MoSe$_2$ (-0.3 V vs. NHE) than the redox potential of O$_2$/•O$_2^-$ (-0.33 V vs. NHE)[49]. Therefore, the •O$_2^-$ should be the reaction product between the photoinduced electrons on the CB of Vs-ZIS and O$_2$ (the CB potential of Vs-ZIS is about -1.10 eV, lager than the redox potential of O$_2$/•O$_2^-$), indicating that a mass of photogenerated electrons were accumulated on the CB of Vs-ZIS under irradiation of visible light, which should be contributed by the recombination between the electron on the CB of MoSe$_2$ and the hole on the VB of Vs-ZIS, thus verifying the direct Z-scheme charge migration mechanism. Above SPV and ESR spin-trapping technique provides the direct proof for the direct Z-scheme charge transfer mechanism inside the Vs-ZIS/MoSe$_2$ photocatalyst.

In summary, we have successfully demonstrated an interfacial Mo-S bond and internal electric field modulated Z-scheme Vs-ZnIn$_2$S$_4$/MoSe$_2$ photocatalyst through a defect-induced heterostructure constructing strategy for boosting the photocatalytic H$_2$ evolution performance. The internal electric field provide the necessary driving force steering the photogenerated electrons on the conduction band of MoSe$_2$ transfer to the valence band of Vs-ZnIn$_2$S$_4$ following the Z-scheme mechanism, while the interfacial Mo-S bond creates direct charge transfer channels between Vs-ZnIn$_2$S$_4$ and MoSe$_2$, further accelerates the Z-scheme charge transfer process. What's more, the abundant S-vacancies also contribute to the enhanced light absorption and accelerated photocarriers separation. The above factors together lead to the outstanding photocatalytic performance of the Vs-ZnIn$_2$S$_4$/MoSe$_2$. Specifically, the optimized photocatalyst exhibits a high AQY of 76.48% at 420 nm, and an ultrahigh H$_2$ evolution rate of 63.21 mmol·g^{-1}•h^{-1} under visible light (λ > 420 nm), which is about 18.8 times higher than that of pristine ZnIn$_2$S$_4$. Besides, the Vs-ZnIn$_2$S$_4$/MoSe$_2$ also shows favorable recycling stability by remaining above 90% rate retention after 20 h of 5 continuous photocatalytic tests. This work not only provides an efficient direct Z-scheme ZnIn$_2$S$_4$-based heterostructure photocatalyst, but also affords a beneficial prototype for designing other Z-scheme photocatalyst for efficient green energy conversion.

Methods

Materials. Analytical grade reagents were used directly without purification. Zinc acetate dihydrate $(Zn(CH_3COO)_2 \cdot 2H_2O)$ was bought from Tianjin guangcheng chemical reagent Co. LTD. Thioacetamide (TAA), Indium chloride $(InCl_3)$, and Selenium power (Se, $\geq$99.99% metal basis) were bought from Shanghai Macklin biochemical technology Co. LTD. Ascorbic acid (AA), 1,5-diphenylcarbazide (DPC), sulfuric acid (H_2SO_4) and hydrazine monohydrate $(N_2H_4 \cdot H_2O, 85\%)$ were bought from Sinopharm Chemical Reagent Co., LTD. Sodium molybdate dihydrate $(Na_2MoO_4 \cdot 2H_2O)$ was purchased from Tianjin Fengchuan Chemical Reagent Technology Co., LTD. Potassium dichromate $(K_2Cr_2O_7)$ was bought from Jinan Reagent Factory. Deionized water was obtained from local sources.

Synthesis of $ZnIn_2S_4$ and Vs-$ZnIn_2S_4$. In a representative experiment, $InCl_3$ (1 mmol), $Zn(CH_3COO)_2 \cdot 2H_2O$ (0.5 mmol), and TAA (4 mmol) were orderly dissolved into 50 mL deionized water, and then stirred at room temperature for 30 minutes. Thereafter, the clear solution was poured into 100 mL stainless steel autoclave, and maintained at 180 ºC oven for 18 hours. After cooling naturally to indoor temperature, the sediment was separated by centrifugation, followed by washing with deionized water and ethanol, and drying at 60 ºC for 10 hours. The obtained yellow powder $ZnIn_2S_4$ were labeled as ZIS. Vs-$ZnIn_2S_4$ was prepared via a $N_2H_4 \cdot H_2O$-assisted hydrothermal method. Typically, 100 mg the as-synthesized ZIS was dispersed into 20 mL deionized water for 1 hour, then, 5 mL $N_2H_4 \cdot H_2O$ was added into the mixing solution and stirred for another 30 minutes. After that, the mixture was transfer to 50 mL stainless steel autoclave, and maintained at 240 ºC oven for 5 hours. Finally, the precipitate was separated by centrifugation, and washing with deionized water for several times, then drying at 60 ºC for 10 hours. The obtained light-yellow powder was labeled as Vs-ZIS.

Synthesis of Vs-$ZnIn_2S_4$/$MoSe_2$ heterostructure. The Vs-$ZnIn_2S_4$/$MoSe_2$ heterostructure were synthesized by the similar process with Vs-$ZnIn_2S_4$, except that $Na_2MoO_4 \cdot 2H_2O$ and Se powders were added into the mixture. The Vs-$ZnIn_2S_4$/$MoSe_2$ with different mass ratio of $MoSe_2$ to $ZnIn_2S_4$ (0.5%, 1.0%, 3.0%, 5.0% and 7.0%) were synthesized by adjusting the addition of $Na_2MoO_4 \cdot 2H_2O$ and Se, and the synthesized samples were labeled as Vs-ZIS/0.5$MoSe_2$, Vs-ZIS/1.0$MoSe_2$, Vs-ZIS/3.0$MoSe_2$, Vs-ZIS/5.0$MoSe_2$, Vs-ZIS/7.0$MoSe_2$, respectively. For comparison, the pure $MoSe_2$ was prepared following the above steps without adding ZIS. Besides, the Vs-ZIS-5.0$MoSe_2$ mixture was also fabricated by ultrasonic mixing the Vs-ZIS with $MoSe_2$ for 1 hour.

Characterization. The morphology and microstructure were investigated by SU8010 scanning electron microscope (SEM) outfitted with an energy dispersive X-ray spectrometer (EDS), and JEM-2100 plus transmission electron microscope (TEM). The crystalline and phase information were characterized by Bruker D8 Advance X-ray diffraction (XRD). The chemical states were investigated by Thermo ESCALAB 250 XI X X-ray photoelectron spectroscopy (XPS, monochromatic Al Kα radiation). The light absorption property was researched by the PerkinElmer Lambda 750S UV-vis spectrophotometer using barium sulfate as standard reference. The recombination of photogenerated carriers was tested by F-4600 spectrofluorometer (375 nm excitation wavelength). The secondary cutoff binding energy was measured

by AXIS SUPRA X-ray photoelectron spectroscopy with He ⍺ as the excitation source. The surface photovoltage (SPV) measurement were carried out on the system consisting a 500 W Xe lamp source equipped with a monochromator, a lock-in amplifier with a light chopper, a photovoltaic cell, and a computer. The Raman spectra were conducted on LabRAM HR Evolution Raman spectrometer with 325 nm excitation wavelength to analysis the composition. The electron paramagnetic resonance (EPR) measurement was conducted on JEOL JES-FA200 EPR spectrometer with a 9.054 GHz magnetic field. The 5,5-dimethyl-pyrroline N-oxide (DMPO) was adopted as spin-trapping reagent and the $\cdot O_2^-$ and $\cdot OH$ were tested in methanol and aqueous solution, respectively.

Photocatalytic water splitting for hydrogen evolution. The hydrogen production experiments were proceeded on Labsolar-6A (PerfectLight, Beijing). Typically, photocatalyst (50 mg) was ultrasonically suspended into 100 mL solution involving 0.1M ascorbic acid sacrificial agent. Prior to exerting light, the reaction system was degassed for 1 hour to thoroughly exclude the air and the dissolved oxygen in reaction system. Then the reaction was proceeded under PLS-SEX300D 300 W Xenon lamp (Perfectlight, Beijing) with a 420 nm cut-off filter. The light intensity was determined by PLMW2000 photoradiometer (Perfectlight, Beijing) to be about 254 mW/cm^2. The generated hydrogen was analyzed by GC 7900 gas chromatograph (Techcomp, 5 Å molecular sieve stainless steel packed column, Ar as carrier gas and TCD detector).

Photoelectrochemical and electrochemical measurements. All the electrochemical and photoelectrochemical measurements were conducted by a three-electrode system on CHI-660E electrochemical workstation. In the typical three-electrode system, the working electrode was a piece of nickel foam coating with the as-prepared photocatalyst, the reference electrode was Hg/HgO, while the counter electrode was Pt wire. The electrolyte was 0.5 M Na_2SO_4 aqueous solution. The electrochemical impedance spectroscopy (EIS) was conducted under open-circuit potential with 0.01 to 1×10^5 Hz frequency range and 0.005 V AC amplitude. The photocurrent response was tested under FX-300 Xe lamp. Mott-Schottky (M-S) plots were collected from -1 to -0.2 V under 10 kHz frequency and 0.01 V amplitude.

The working electrode was fabricated as follows: a certain amount of photocatalyst, carbon black and polyvinylidene fluoride were weighted according to the mass ratio of 8:1:1, and then dispersed into N-methyl-2-pyrrolidone to gain a homogeneous paste. The paste was daubed on a piece of pre-cleaned 1×1 cm^2 FTO collector, and then dried in 60 °C vacuum for 1 hour.

Declarations

Acknowledgements

Author contributions

X.W(1)., A.M. and Z.L. conceived the research. X.W(1). and X.W(2). prepared photocatalysts and conducted all the experiments. X.W(2). and J.H. performed the electrochemistry measurement. S.L. offered help to analyze the characterization experiment data. X.W(1)., X.W(2). and Z.L. wrote and revised the manuscript. A.M., S.L. and J.H. gave suggestions on the experiment and writing.

Competing interests

The authors declare no conflict of interest.

Additional Information

Table S1-S7 and Fig. S1-S8.

References

1. Hisatomi, T. & Domen, K. Reaction systems for solar hydrogen production via water splitting with particulate semiconductor photocatalysts. *Nat. Catal.* **2**, 387-399 (2019).

2. Dai, B. Y. et al. Construction of Infrared-Light-Responsive Photoinduced Carriers Driver for Enhanced Photocatalytic Hydrogen Evolution. *Adv. Mater.* **32**, 1906361 (2020).

3. Zhu, Q. H. et al. Dopant-Induced Edge and Basal Plane Catalytic Sites on Ultrathin C_3N_4 Nanosheets for Photocatalytic Water Reduction. *ACS Sustainable Chem. Eng.* **8**, 7497-7502 (2020).

4. Kosco, J. et al. Enhanced photocatalytic hydrogen evolution from organic semiconductor heterojunction nanoparticles. *Nat. Mater.* **19**, 559-565 (2020).

5. Yu, P. et al. Earth abundant materials beyond transition metal dichalcogenides: A focus on electrocatalyzing hydrogen evolution reaction. *Nano Energy.* **58** 244-276 (2019) .

6. Wang, Z. Inoue, Y. Hisatomi, T. Ishikawa, R. Wang, Q. Takata, T. Chen, S. Shibata, N. Ikuhara, Y. & Domen, K. Overall water splitting by Ta_3N_5 nanorod single crystals grown on the edges of $KTaO_3$ particles. *Nat. Catal.* **1**, 756-763 (2018).

7. Yu, H. Huang, J. Jiang, L. Shi, Y. Yi, K. Zhang, W. Zhang, J. Chen, H. & Yuan,X. Enhanced photocatalytic tetracycline degradation using N-CQDs/O_V-BiOBr composites: Unraveling the complementary effects between N-CQDs and oxygen vacancy. *Chem. Eng. J.* **402**, 126187 (2020).

8. Wang, J. Chen, Y. Zhou, W. Tian, G. Xiao, Y. Fu, H. & Fu, H. Cubic quantum dot/hexagonal microsphere $ZnIn_2S_4$ heterophase junctions for exceptional visible-light-driven photocatalytic H_2 evolution. *J. Mater. Chem. A.* **5**, 8451-8460 (2017).

9. Gao, D. Wu, X. Wang, P. Yu, H. Zhu, B. Fan, J. & Yu, J. Selenium-enriched amorphous $NiSe_{1+x}$ nanoclusters as a highly effcient cocatalyst for photocatalytic H_2 evolution. *Chem. Eng. J.* **408**, 127230 (2020).

10. Rao, F. Zhua, G. Zhang, W. Gao, J. Zhang, F. Huang, Y. Mirabbos Hojamberdieve. In-situ generation of oxygen vacancies and metallic bismuth from $(BiO)_2CO_3$ via N_2-assisted thermal-treatment for efcient selective photocatalytic NO removal. *Appl. Catal. B Environ.* **281**, 119481 (2021).

11. Wang, Y. Shang, X. Shen, J. Zhang, Z. Wang, D. Lin, J. Wu, J. Fu, X. Wang, X. & Li, C. Direct and indirect Z-scheme heterostructurecoupled photosystem enabling cooperation. of CO_2 reduction and H_2O oxidation. *Nat. Commun.* **11**, 3043 (2020).

12. Wu, Z. Zhao, Y. Jin, W. Jia, B. Wang, J. & Ma, T. Recent Progress of Vacancy Engineering for Electrochemical Energy Conversion Related Applications. *Adv. Funct. Mater.* 2009070 (2020).

13. Yang, F. et al. Facile oxalic acid-assisted construction of laminated porous N-deficient graphitic carbon nitride: Highly efficient visible-light-driven hydrogen evolution photocatalyst. *J. Energy. Chem.* **33**, 1-8 (2019).

14. Wang, Y. Chen, D. Qin, L. Liang, J. & Huang, Y. Hydrogenated $ZnIn_2S_4$ microspheres: boosting photocatalytic hydrogen evolution by sulfur vacancy engineering and mechanism insight. *Phys. Chem. Chem. Phys.* **21**, 25484-25494 (2019).

15. Wang, J. Yang, L. & Zhang, L. Constructed 3D hierarchical micro-flowers $CoWO_4$@Bi_2WO_6 Z-scheme heterojunction catalyzer: Two-channel photocatalytic H2O2 production and anti-biotics degradation. *Chem. Eng. J.* 127639 (2020)

16. Gu, Y. et al. Two Dimensional Porous Molybdenum Phosphide/Nitride Heterojunction Nanosheets for pH-Universal Hydrogen Evolution Reaction. *Angew. Chem. Int. Ed.* (2020).

17. Wu, J. et al. Piezotronic effect boosted photocatalytic performance of heterostructured $BaTiO_3$/TiO_2 nanofbers for degradation of organic pollutants. *Nano Energy.* **77**, 105122 (2020).

18. Xu, H. et al. Metal-Oxide-Mediated Subtractive Manufacturing of Two-Dimensional Carbon Nitride for High-Efficiency and High-Yield Photocatalytic H_2Evolution. *ACS nano.* **13**, 11294-11302 (2019).

19. Chao, Y. et al. Ultrathin Visible-Light-Driven Mo Incorporating In_2O_3-$ZnIn_2Se_4$ Z-Scheme Nanosheet Photocatalysts. *Adv. Mater.* **31**, 1807226 (2019).

20. Kwon, I. S. et al. Se-Rich $MoSe_2$ Nanosheets and Their Superior Electrocatalytic Performance for Hydrogen Evolution Reaction. *ACS Nano.* **14**, 6295-6304 (2020).

21. Li, Z. et al. CoNi Bimetal Cocatalyst Modifying a Hierarchical $ZnIn_2S_4$ Nanosheet-Based Microsphere Noble-Metal-Free Photocatalyst for Efficient Visible-Light-Driven Photocatalytic Hydrogen Production. *ACS Sustain. Chem. Eng.* **7,** 20190-20201 (2019).

22. Yang, M. Q. et al. Self-surface charge exfoliation and electrostatically coordinated 2D hetero-layered hybrids. *Nat. Commun.* **8,** 14224 (2017).

23. Zeng, D. et al. Hierarchical $ZnIn_2S_4/MoSe_2$ Nanoarchitectures for Efficient Noble-Metal-Free Photocatalytic Hydrogen Evolution under Visible Light. *ChemSusChem.* **10**, 4624-4631 (2017).

24. Zhang, S. et al. Atomic-Level and Modulated Interfaces of Photocatalyst Heterostructure Constructed by External Defect-Induced Strategy: A Critical Review. *Small.* **17**, 2004980 (2020).

25. Tao, X. et al. Interfacial Charge Modulation: An Efficient Strategy for Boosting Spatial Charge Separation on Semiconductor Photocatalysts. *Adv. Energy Mater.* **9**, 1803951 (2019).

26. Guo, Y. Shi, W. & Zhu, Y. Internal electric field engineering for steering photogenerated charge separation and enhancing photoactivity. *EcoMat.*1 (2019).

27. Wang, Y. et al. Construction of Z-scheme $MoSe_2/CdSe$ hollow nanostructure with enhanced full spectrum photocatalytic activity. *Appl. Catal. B Environ.* **244**, 76-86 (2019).

28. Liu, T. T. et al. Dynamic photocatalytic membrane coated with $ZnIn_2S_4$ for enhanced photocatalytic performance and antifouling property. *Chem. Eng. J.* **379** 122379 (2020).

29. Vikraman, D. et al. Engineering the novel $MoSe_2-Mo_2C$ hybrid nanoarray electrodes for energy storage and water splitting applications. *Appl. Catal. B Environ.* **264**, 118531 (2020).

30. Li, F. et al. High-performance optoelectronic devices based on van der Waals vertical $MoS_2/MoSe_2$ heterostructures. *Nano Res.***13,**1-7 (2020).

31. Cheng, C. et al. Facile preparation of nanosized MoP as cocatalyst coupled with $g-C_3N_4$ by surface bonding state for enhanced photocatalytic hydrogen production. *Appl. Catal. B Environ.* **265**, 118620 (2020).

32. Huang, X. et al. Recent advances of doped graphite carbon nitride for photocatalytic reduction of CO_2: a review. *Res. Chem. Intermed.* **46**, 5133-5164 (2020).

33. Du, C. et al. Half-unit-cell $ZnIn_2S_4$ monolayer with sulfur vacancies for photocatalytic hydrogen evolution. *Appl. Catal. B Environ.* **248**,193-201 (2019).

34. Zhang, S. et al. MoS_2 Quantum Dot Growth Induced by S Vacancies in a $ZnIn_2S_4$ Monolayer: Atomic-Level Heterostructure for Photocatalytic Hydrogen Production. *ACS nano.* **12**, 751-758 (2018).

35. Wang, Y. Z. et al. Hydrogenated $ZnIn_2S_4$ microspheres: boosting photocatalytic hydrogen evolution by sulfur vacancy engineering and mechanism insight. *Phys.Chem.Chem.Phys.* **21**, 25484 (2019).

36. Ma, Y. W. et al. Carbon inserted defect-rich MoS_{2-X} nanosheets@CdSnanospheres for efficient photocatalytic hydrogen evolution under visible light irradiation. *Colloid Interface Sci.* **569,** 89-100 (2020).

37. Fan, L. L. et al. Controllable S-Vacancies of monolayered Mo−S nanocrystals for highly harvesting lithium storage. *Nano energy.* **78,** 105235 (2020).

38. Turner, N. H. & Singlet, A. M. Determination of peak positions and areas from wide-scan XPS spectra. *Surf Interface Anal.* **15**, 215-222 (1990).

39. Vikraman, D. et al. Engineering the novel MoSe$_2$-Mo$_2$C hybrid nanoarray electrodes for energy storage and water splitting applications. *Appl. Catal. B Environ.* **264**, 118531 (2020).

40. Xu, F. et al. Unique S-scheme heterojunctions in selfassembled TiO$_2$/CsPbBr$_3$ hybrids for CO$_2$ photoreduction. *Nat.Commun.* **11**, 4613 (2020).

41. Li, P. S. et al. Visible-Light-Driven Nitrogen Fixation Catalyzed by Bi$_5$O$_7$Br Nanostructures: Enhanced Performance by Oxygen Vacancies *J. Am. Chem. Soc.* **142**, 12430-12439 (2020).

42. Zhang, L. Hao, X. Wang, Y. Jin, Z. & Ma, Q. Construction strategy of Mo-S@Mo-P heterojunction formed with in-situ phosphating Mo-S nanospheres toward efficient photocatalytic hydrogen production. *Chem. Eng. J.* **391**, 123545 (2020).

43. Xu, W. et al. Interfacial Chemical Bond-Modulated Z-Scheme Charge Transfer for Efcient Photoelectrochemical Water Splitting. *Adv. Energy Mater.* 2003500 (2021).

44. Shen, R. Zhang, L. Chen, X. Jaroniec, M. Li, N. & Li, X. Integrating 2D/2D CdS/α-Fe$_2$O$_3$ ultrathin bilayer Z-scheme heterojunction with metallic β-NiS nanosheet-based ohmic-junction for efficient photocatalytic H$_2$ evolution. *Appl. Catal. B Environ.* **266**, 118619 (2020).

45. Qiu, J. Li, M. Yang, L. & Yao, Facile construction of three-dimensional netted ZnIn$_2$S$_4$ by cellulose nanofibrils for efficiently photocatalytic reduction of Cr(VI).J. *Chem. Eng. J.* **375**, 121990 (2019).

46. Lin, Y. et al. The Evolution from a Typical Type-I CdS/ZnS to Type-II and Z-Scheme Hybrid Structure for Efficient and Stable Hydrogen Production under Visible Light. *ACS Sustain. Chem. Eng.* **8**, 4537-4546 (2020).

47. Geng, Y. X. et al. Z-Scheme 2D/2D α-Fe$_2$O$_3$/g-C$_3$N$_4$ heterojunction for photocatalytic oxidation of nitric oxide. *Appl. Catal. B Environ.* **280**,119409 (2021).

48. Zhao, Z. et al. Recycling of spent alkaline Zn-Mn batteries directly: Combination with TiO$_2$ to construct a novel Z-scheme photocatalytic system. *J. Hazard. Mater.* **400**,123236 (2020).

49. Zhu, Q. H. et al. Electron directed migration cooperated with thermodynamic regulation over bimetallic NiFeP/g-C$_3$N$_4$ for enhanced photocatalytic hydrogen evolution. *Appl. Catal. B Environ.* **259**,118078 (2019).

Figures
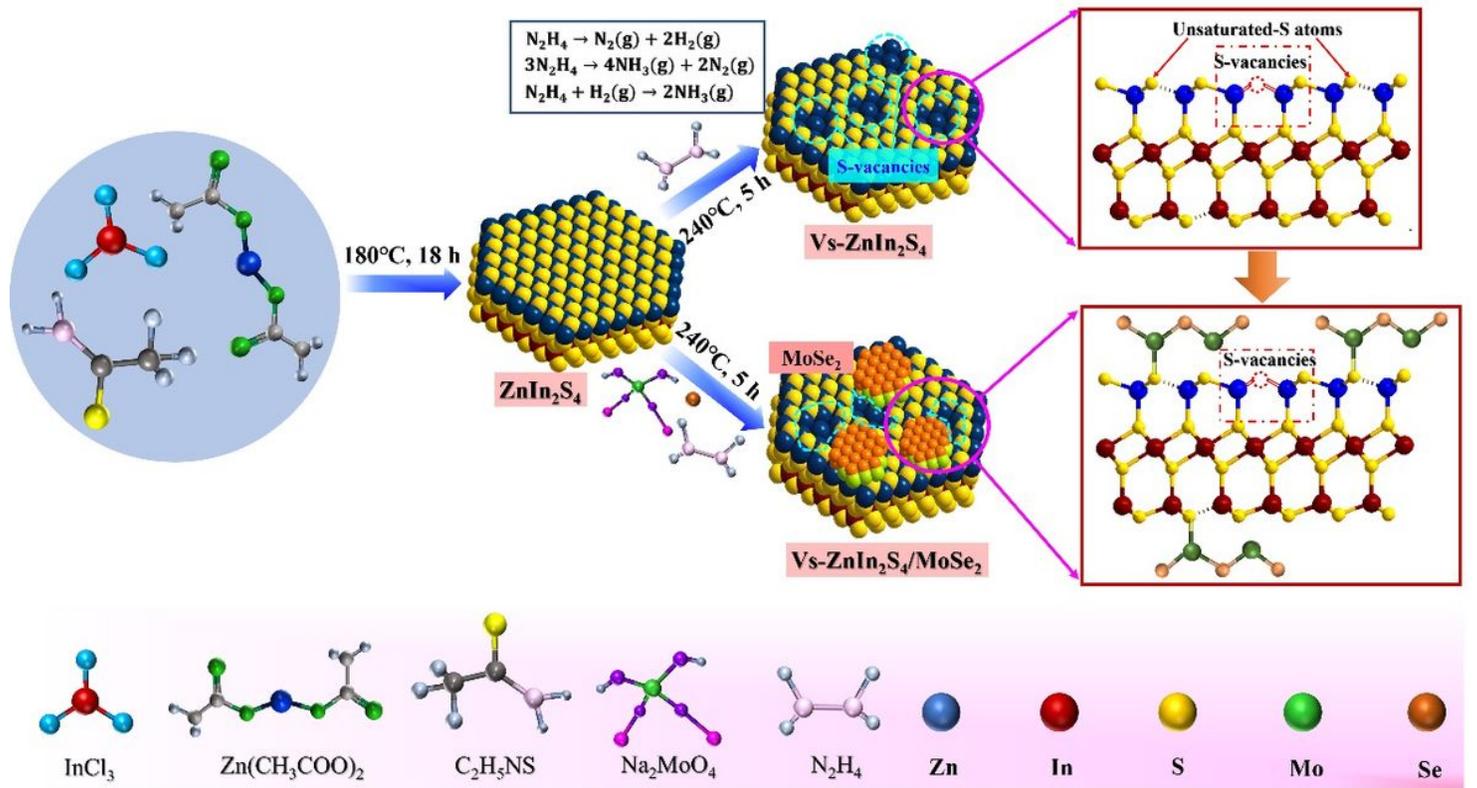
Figure 1

Synthesis process. Schematic presentation of the synthetic route of Vs-ZnIn2S4 and Vs-ZnIn2S4/MoSe2 heterostructure.
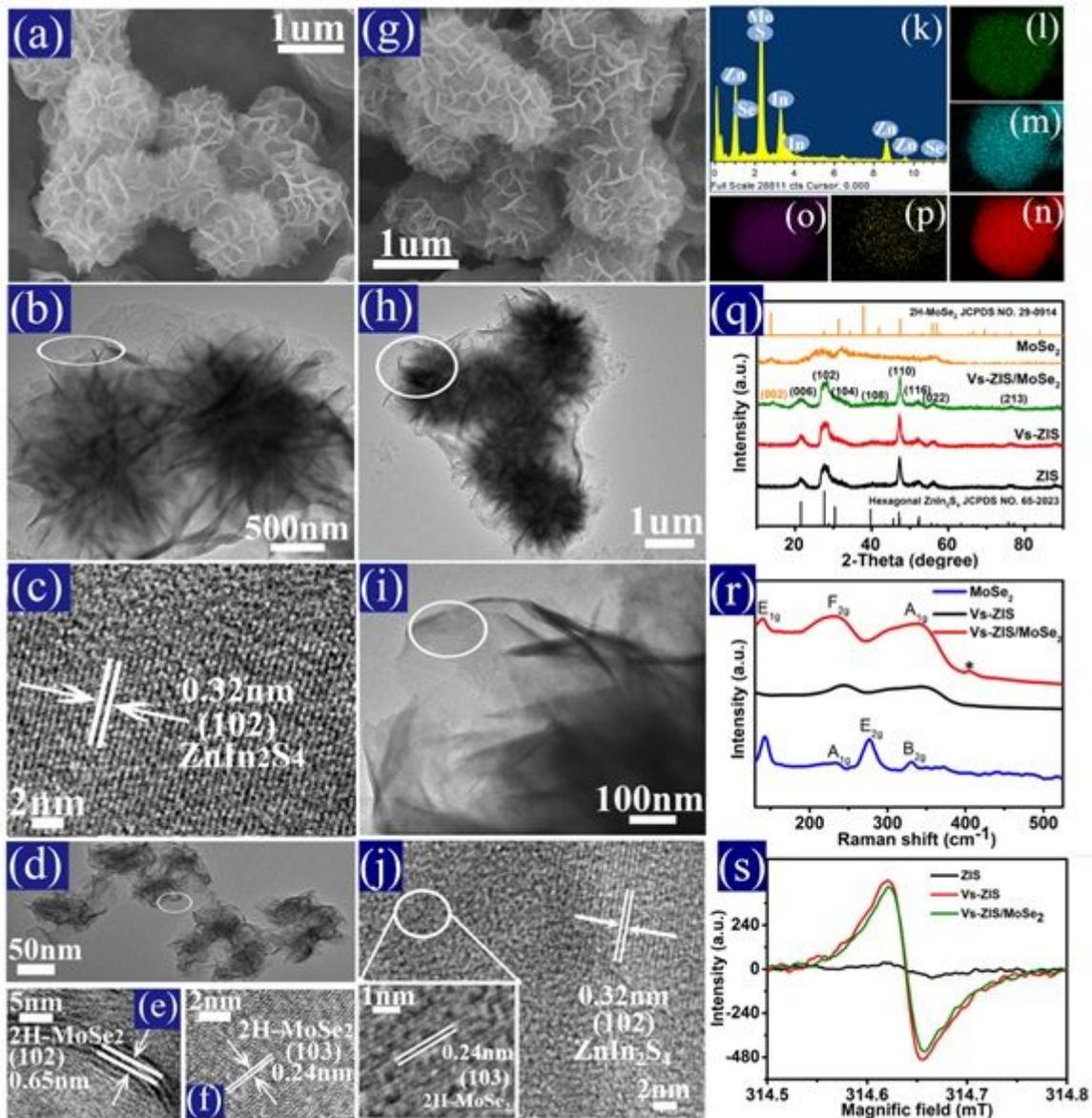
Figure 2

Morphology and composition characterizations. a-c SEM, TEM and HRTEM pictures of ZIS, d-f TEM and HRTEM images of MoSe2, g-j SEM, TEM and HRTEM images of Vs-ZIS/MoSe2, k-p EDS and elements mapping of Zn, In, S, Mo and Se in Vs-ZIS/MoSe2, q XRD patterns of ZIS, Vs-ZIS, MoSe2 and Vs-ZIS/MoSe2, r Raman spectra of Vs-ZIS, MoSe2 and Vs-ZIS/MoSe2, and s EPR spectra of ZIS, Vs-ZIS and Vs-ZIS/MoSe2.
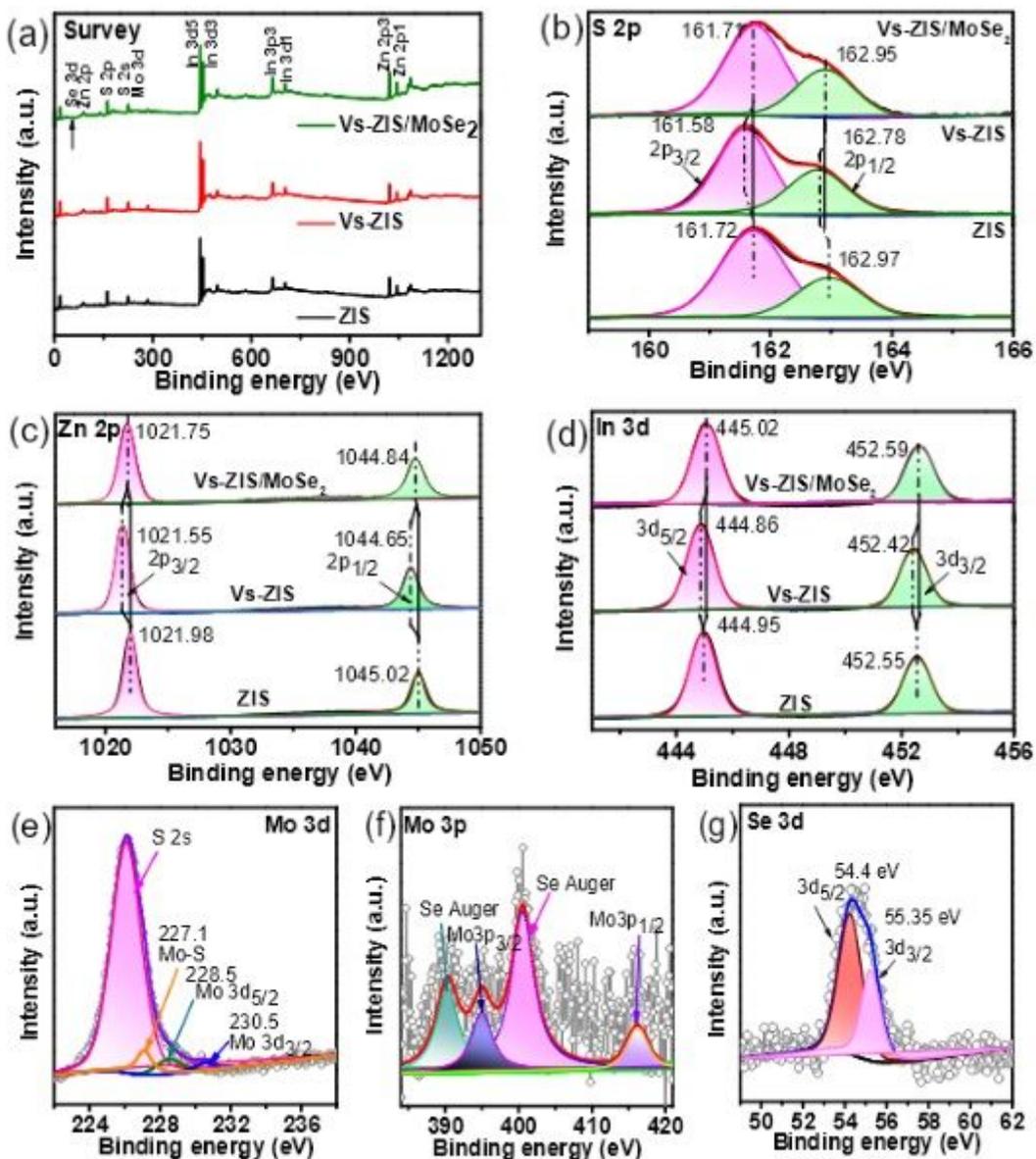
Figure 3

XPS spectra. a survey, b S 2p, c Zn 2p, d In 3d for ZIS, Vs-ZIS and Vs-ZIS/MoSe2, e Mo 3d and S 2s, f Mo 3p and g Se 3d of Vs-ZIS/MoSe2.
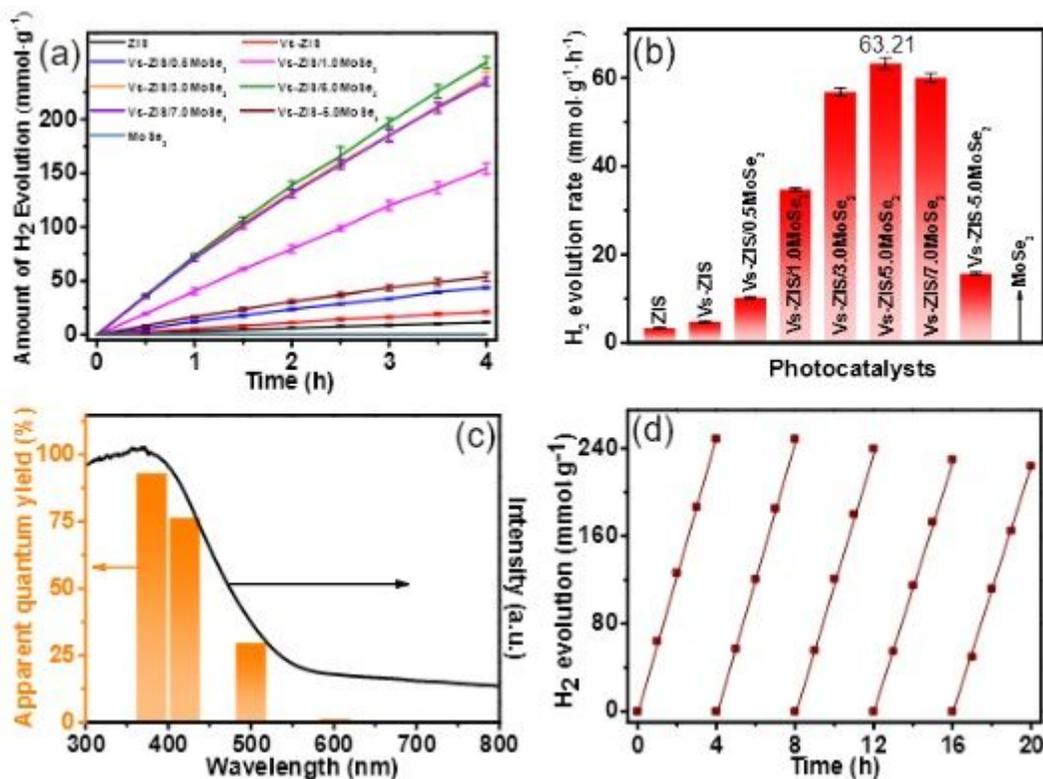
Figure 4

Photocatalytic H2 evolution property. a H2 evolution amount at different irradiation time and b H2 evolution rate of different photocatalysts, c wavelength-dependent apparent quantum yield (AQY) and d cycling stability test of Vs-ZIS/5.0MoSe2.
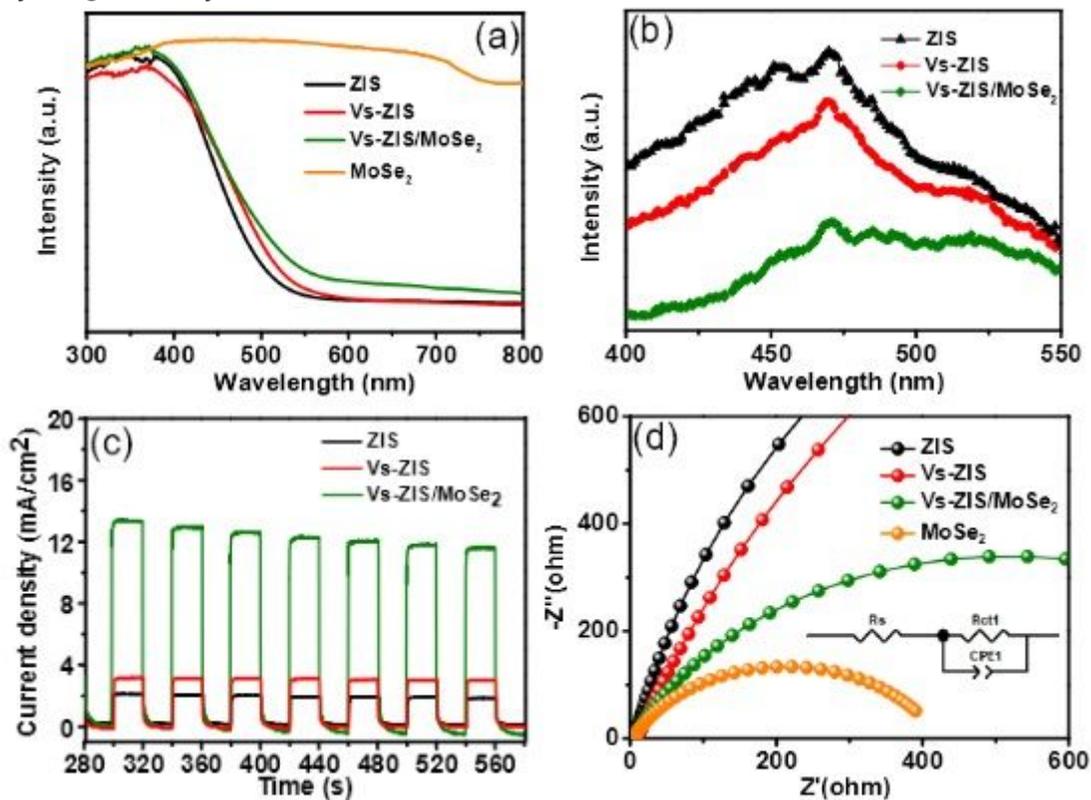
Figure 5

Photophysical and Electrochemical measurements. a UV-vis absorption spectrum, b photoluminescence spectra (PL, excited at 375 nm), c photocurrent response and d electrochemical impedance spectroscopy (EIS) of the as-prepared samples.
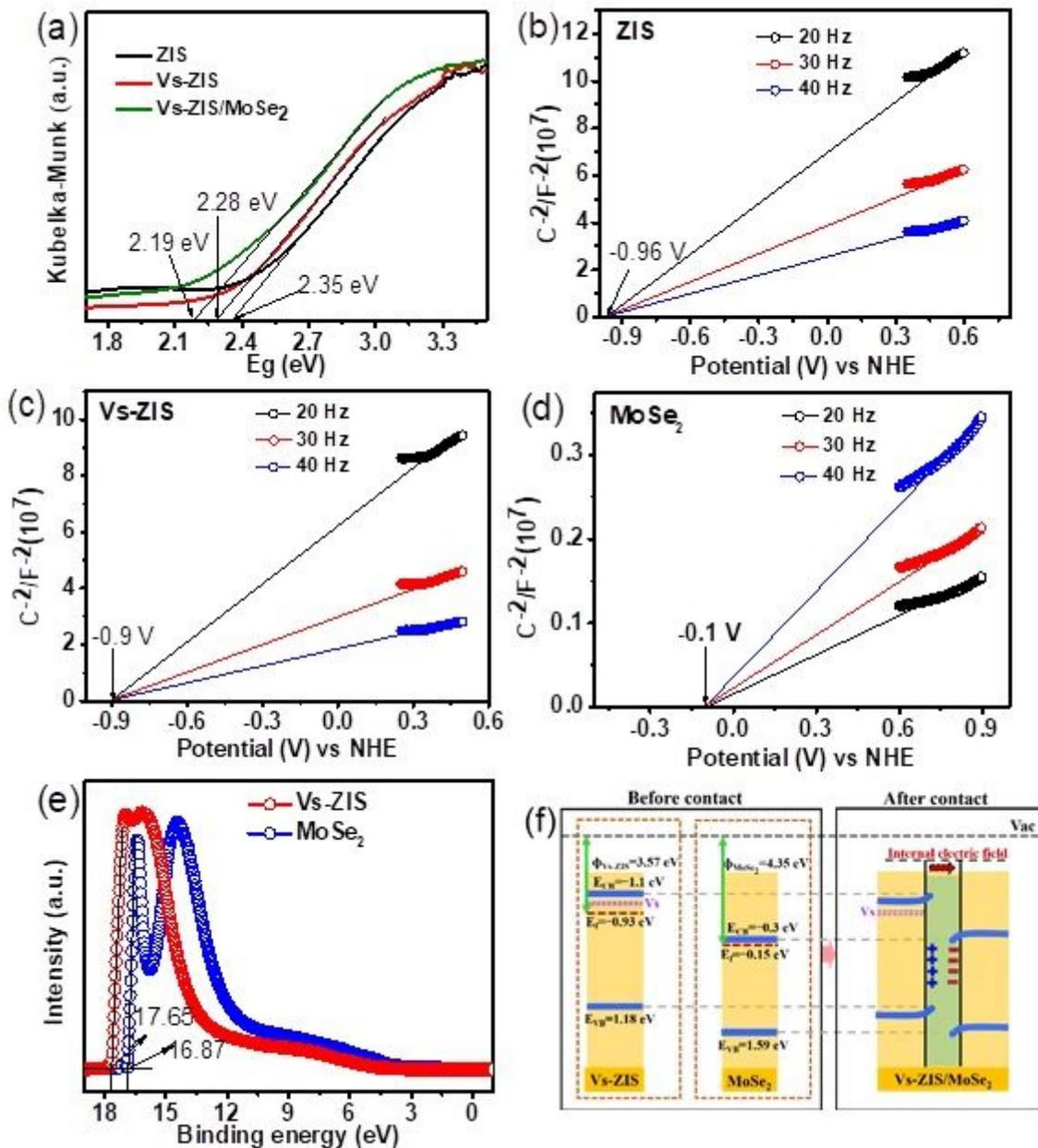
Figure 6

Band structure and the formation of internal electric field. a Kubelka-Munk function vs. the energy of incident light plots, b-d Mott-Schottky (M-S) plot, e UPS spectra of the as-prepared samples, and f band structure of Vs-ZIS, MoSe2 and Vs-ZIS/MoSe2.
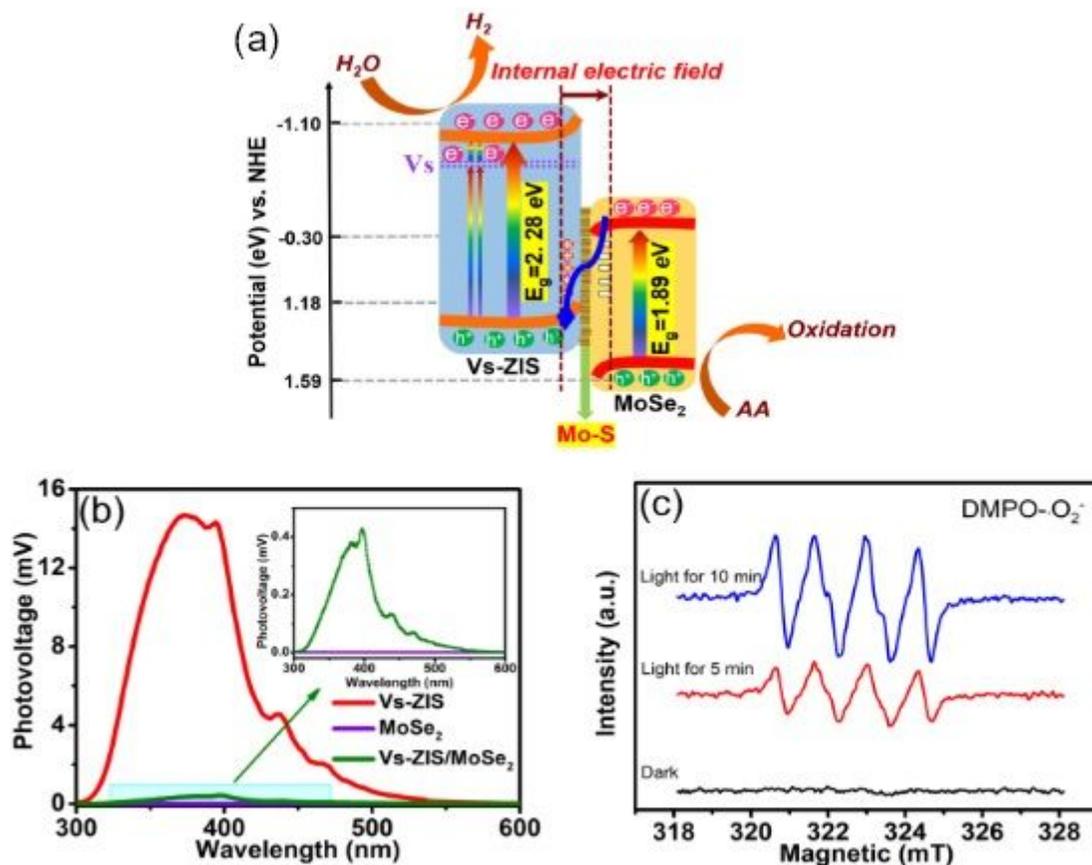
Figure 7

Photocatalytic mechanism and verification. a photocatalytic reaction mechanism of Vs-ZIS/MoSe2 under light irradiation, b Surface photovoltage (SPV) measurement of Vs-ZIS, MoSe2 and Vs-ZIS/MoSe2, and c DMPO spin-trapping EPR spectra of DMPO-•O2- of ZIS/MoSe2 in methanol solution.

Supplementary Files

This is a list of supplementary files associated with this preprint. Click to download.

- SupportingInformation.docx